Simultaneous Retrieval of Diurnal to Seasonal Surface Temperatures and Emissivities over SGP ARM–CART Site Using GOES Split Window

DAVID A. FAYSASH AND ERIC A. SMITH

Department of Meteorology, The Florida State University, Tallahassee, Florida

(Manuscript received 25 September 1998, in final form 9 September 1999)

ABSTRACT

GOES-8 thermal infrared split window measurements have been used with a simultaneous land surface temperature (LST)–spectral emissivity retrieval algorithm to examine the potential of a combined retrieval methodology cast into a variational solution for temperatures at multiple but short-term 6- to 24-h time intervals and emissivities at multiple spectral bands assumed to be invariant over the selected time intervals. Retrieved LST and emissivity quantities under differing atmospheric conditions over an annual cycle are validated and analyzed in regard to their underlying diurnal and seasonal variations over the Department of Energy's Atmospheric Radiation Measurement–Cloud and Radiation Test Bed (ARM–CART) site in Kansas and Oklahoma.

It is shown that the accuracy of the retrieval algorithm depends primarily on GOES infrared channel detector noise and uncertainties in columnar water vapor path, in which retrieval accuracy increases as pathlength decreases. A detailed analysis is given of the characteristic temporal–spatial gradient structures of LSTs and emissivities over the ARM–CART domain at point to area space scales and diurnally to seasonally varying timescales. Emphasis is given to explaining the relationship of heterogeneous features in the retrievals in conjunction with physical attributes of the landscape, that is, ecotones and phenology, and the effects of prior cloudiness on subsequent LSTs.

1. Introduction

Various algorithms have been developed to retrieve the land surface temperature (LST) using equivalent blackbody brightness temperatures (EBBTs) measured in the ''clean'' (~10.5–11.5 μm) and ''dirty'' (~11.5–12.5 μm) spectral bands of the atmospheric split window. Here, clean and dirty refer to the relative intensity of water vapor absorption. The characteristic form of these algorithms is

$$T_s = a_0 T_{11} + a_1 T_{12} + a_2, \qquad (1)$$

where T_{11} and T_{12} are the clean and dirty EBBTs, respectively, and a_0, a_1, and a_2 are empirically, semiempirically, or physically derived coefficients; see Prata et al. (1995) for a review of LST retrieval. Because the coefficients are functions of channel emissivities, accurate LST retrieval depends upon accurate differential emissivity specification. For example, emissivity errors of 5% can lead to LST errors of 2°C or larger (Becker 1987).

Measurements by Nerry et al. (1990), Schmugge et al. (1991), and Rubio et al. (1997) show that channel emissivities are typically dependent upon surface cover conditions, such as the amount of exposed soil and the state of vegetation (green versus water stressed). Because surface conditions can vary within a satellite pixel, across a satellite image, and through the course of time, one of the challenges in implementing LST algorithms is providing accurate emissivity specification. For well-vegetated surfaces, Prata (1994) suggests using invariant channel emissivities of 0.98. For heterogeneous pixels, Caselles et al. (1997) estimated channel emissivities using the average of invariant vegetation and soil emissivities weighted by fractional vegetation cover. The latter term was estimated from Normalized Difference Vegetation Indices (NDVI), calculated from visible and near-infrared radiances; characteristic soil and vegetation emissivities were assigned from in situ measurements.

As an alternative to specifying emissivities, a few algorithms have been developed to simultaneously retrieve emissivities and LSTs. By treating the earth's surface as a homogenous Lambertian reflector, the radiance measured by a satellite in any thermal infrared channel ''i'' can be expressed as

$$I_i = \varepsilon_i \tau_i B_i(T_s) + I_i^{\uparrow} + (1 - \varepsilon_i)\tau_i I_i^{\downarrow}, \qquad (2)$$

where ε_i is the channel emissivity, $B_i(T_s)$ is the Planck function evaluated at the surface temperature T_s, τ_i is the atmospheric transmittance, $I_i^{\uparrow}$ is the atmospheric

Corresponding author address: Dr. Eric A. Smith, Dept. of Meteorology, The Florida State University, Tallahassee, FL 32306-4520. E-mail: esmith@metsat.met.fsu.edu

upwelling radiance, and $I_i\downarrow$ is the downwelling radiance appearing in the earth's surface reflectance term. If the atmospheric effects (τ_i, $I_i\uparrow$, $I_i\downarrow$) can be calculated, then (2) represents a system of n equations and $n + 1$ unknowns (n channel emissivities and one LST) for radiances measured in n channels. Simultaneous retrieval algorithms close this system by introducing n channel radiances measured at a second time and assuming that the channel emissivities remain invariant across the sampling interval. This allows n channel emissivities and two LSTs to be retrieved.

Watson (1992) first proposed this idea and employed it for Thermal Infrared Multispectral Scanner (TIMS) data. Two other studies followed their lead. The thermal infrared spectral index (TISI) method of Li and Becker (1993) used day and night Advanced Very High Resolution Radiometer (AVHRR) near-infrared (3.7 μm) and infrared (10.8 and 11.9 μm) measurements to retrieve spectral emissivities for use with the Becker and Li (1990) LST algorithm. Xiang and Smith (1997) used a least squares optimization approach to retrieve LSTs and emissivities at 19, 37, and 85 GHz (vertically–horizontally polarized) for the Special Sensor Microwave Imager (SSM/I).

In the lead paper of this study, Faysash and Smith (1999) developed a physically based least squares optimization algorithm for retrieving emissivities and LSTs from atmospheric corrected radiance measurements, primarily for the GOES imager (hereinafter referred to as the FS-98 algorithm). Note that GOES also measures in the near-infrared at 3.78–4.03 μm, which enables the Li and Becker (1993) TISI method to be used for emissivity retrieval. The main advantages of the FS-98 algorithm over the latter two simultaneous algorithms are its lack of dependence on near-infrared information (which contains solar reflectance during daytime), and the resolution afforded by infrared sensors over diffraction-limited passive microwave radiometers.

In the Faysash and Smith (1999) study, biases and bias-adjusted root-mean-square errors (rmse) were found to be less than 2° and 5°C for a set of high-quality validation sites (vegetated canopies) tested with both *GOES-8* and AVHRR versions of the algorithm. Time-averaged retrieved emissivities were found to be between 0.94 and 0.98 for these sites. Although coincident emissivity measurements were not available, this range of values is consistent to that found in the literature for vegetated surfaces.

One of the common problems with the published simultaneous retrieval studies is that the algorithms have not been applied to extensive datasets in attempts to diagnose their robustness with respect to variable space–time conditions and the varying degree of heterogeneity in land surface properties. The objectives of this study are to examine the behavior of the FS-98 algorithm for differing atmospheric–surface cover conditions and to determine the prominent features of land surface temperature and emissivity across various timescales (diurnal and seasonal) and space scales (pixel scale and regional scale) for a space domain containing an adequate network of validation sites.

As with the FS-98 study, we continue to use *GOES-8* split window measurements (channels 4 and 5). Also, the Department of Energy's Atmospheric Radiation Measurement–Cloud and Radiation Test Bed site called ARM–CART (Stokes and Schwartz 1994) serves as the main study area. A description of data used for the study is given in section 2. The simultaneous retrieval algorithm is described in section 3 along with its sensitivity to atmospheric correction errors and satellite channel noise. Results of the validation portion of this study are presented in section 4. The diurnal to seasonal behavior of the LST fields and the seasonal behavior of the emissivity fields over ARM–CART are presented in section 5. Final conclusions are offered in section 6.

2. Study area and datasets

The variable atmospheric–surface cover conditions and extensive observational network make ARM–CART an ideal location for retrieval studies. ARM–CART encompasses an approximately 400 × 400 km area within Kansas and Oklahoma (see Fig. 2 in Faysash and Smith 1999). Land use maps (A. Ciallea 1998, personal communication) indicate that ARM–CART is mainly composed of grasslands, rangelands, and agricultural fields. NDVI maps produced by Gao et al. (1998) for ARM–CART show a seasonal cycle in green vegetation mass, with maximum amounts occurring in summer and little in winter. Since there are agricultural lands within the region, the amount of exposed soil changes with growing season for those portions of the study area under tillage. To capture the seasonal changes in atmospheric and surface cover conditions, retrievals were made for four evenly spaced calendar months in 1996 and 1997 (September and December 1996, March and June 1997). Table 1 gives a summary of average atmospheric conditions.

The satellite data consist of *GOES-8* channel 4 and 5 split window infrared (IR) measurements (10.2–11.2 and 11.5–12.5 μm, respectively). The pixel size for the GOES IR measurements is 2.3 × 4.0 km at nadir, with a 4-km nominal (nadir) ground resolution such that there is oversampling along the east–west scan-sweep axis and contiguous sampling along the north–south mirror-step axis. The noise equivalent delta radiances (NEΔN) for channels 4 and 5 are 0.31 and 0.35 mW m^{-2} sr^{-1}, respectively; see Kidder and Vonder Haar (1995). Throughout 1998, GOES images were collected for ARM–CART by The Florida State University Direct Readout Ground Station at a frequency of twice per hour, with the exception of September and March when GOES operations ceased between 0300 and 0700 UTC daily (because the satellite's solar energy source was eclipsed by the earth). Within each month there were

TABLE 1. Study-period mean atmospheric conditions consisting of precipitable water, atmospheric temperature,* measured AERI downward radiances, and calculated MODTRAN downward radiances (Ch = channel).

Study period	Precipitable water (g cm^{-2})	Atmospheric temperature (K)	Measured downward radiance Ch 4 (mW m^{-2} sr^{-1} cm)	Measured downward radiance Ch 5 (mW m^{-2} sr^{-1} cm)	MODTRAN downward radiance Ch 4 (mW m^{-2} sr^{-1} cm)	MODTRAN downward radiance Ch 5 (mW m^{-2} sr^{-1} cm)
1	2.83	291	28.42	50.35	29.28	50.70
2	2.20	286	14.86	28.15	16.93	30.35
3	1.45	284	9.22	18.05	10.78	19.61
4	1.35	279	N/A	N/A	6.50	13.70
5	1.35	282	10.12	19.16	10.45	19.04
6	0.8	278	4.33	8.40	5.02	8.64
7	0.7	285	6.89	12.93	7.70	13.30
8	1.38	287	11.48	21.31	11.37	20.77
9	2.22	287	N/A	N/A	28.60	49.59
10	1.86	287	N/A	N/A	27.63	47.97
11	3.45	290	33.66	65.06	30.31	51.41
12	3.12	295	N/A	N/A	54.53	83.93
13	3.50	289	55.60	75.80	40.63	66.08
14	4.13	291	56.38	84.71	48.34	75.71

* Mean value theorem allows atmospheric temperature (T_a) to be calculated from atmospheric upward radiance ($L_4\uparrow$) and transmittance (τ_4) according to $B_4(T_a) = L_4\uparrow/(1 - \tau_4)$. Note N/A indicates AERI radiances were unavailable.

several cloud-free or partially cloudy study periods suitable for retrieval (see Table 2).

Atmospheric correction was done using the MODTRAN 3.5 radiative transfer model (Berk et al. 1989) with radiosonde profiles obtained from the ARM–CART central facility (36.6°N, 97.48°W) used as input. MODTRAN's 1 cm^{-1} spectral output was integrated over the *GOES-8* channel filter functions to obtain channel transmittances and directional radiances. The profiles were available every 3 h beginning at 0200 UTC daily. Linear interpolation of the correction factors were used for satellite images taken between radiosonde launches. Stated uncertainties of the temperature and humidity measurements from the soundings are ±0.2°C and ±2–3%, respectively; see http://www.arm.gov/docs/instruments/static/bbss.html.

In situ skin temperature estimates were obtained from emissivity-corrected upwelling longwave fluxes measured at 18 surface meteorological–energy balance stations located throughout ARM–CART by pyrgeometers mounted at a height of 10 m. The upwelling fluxes ($L\uparrow$) were converted to estimated skin temperatures (T_s) by

$$T_s = \{[L\uparrow - (1 - \varepsilon)L\downarrow]/\varepsilon\sigma\}^{1/4}, \qquad (3)$$

where $L\downarrow$ is a coincident downwelling flux, ε is a broadband emissivity, and σ is the Stefan–Boltzmann constant. Broadband emissivities of 0.98 (green grass; B. L. Blad 1998, personal communication) and 0.966 (dry

TABLE 2. Beginning and ending dates for study periods.

Month	Study period	Beginning day/time (UTC)	Ending day/time (UTC)	Separation (hours)
Sep 1996	1	9/1415	11/1345	24
	2	21/0715	22/0945	12
	3	28/0015	29/2345	24
Dec 1996	4	7/2015	8/1315	6
	5	12/1215	13/2345	12
Mar 1997	6	5/1815	6/1745	6
	7	10/1115	11/0445	6
	8	20/0015	21/2315	36[a]
Jun 1997	9	1/0415	1/1515	6
	10	5/0215	5/1315	8
	11	18/0515	19/0445	6
	12	21/0115	22/0815	24[b]
	13	25/2045	26/2315	24[c]
	14	30/0315	30/1215	5

[a] Images from 20 Mar (day 79)/1345 UTC to 21 Mar (80)/1415 UTC were missing.
[b] Images between 0845 and 2345 UTC on both 21–22 Jun (172–173) not used because of clouds.
[c] Images between 0015 and 1945 UTC on 25 Jun (176) were not used because of clouds.

TABLE 3. Summary of channel emissivities, satellite radiances, skin temperatures,* channel transmittances, and directional radiances used for sensitivity experiment.

Channel	Emissivity	Satellite radiance (mW m^{-2} sr^{-1} cm)	Skin temperature (K)	Channel transmittance (τ_i)	Upwelling radiance $I_i\uparrow$ (mW m^{-2} sr^{-1} cm)	Downwelling radiance $I_i\downarrow$ (mW m^{-2} sr^{-1} cm)
			Midlatitude Winter			
4	0.96	72.322	277	0.9138	5.096	5.188
		86.613	265			
5	0.96	61.108	277	0.8758	9.320	9.546
		74.920	265			
			Midlatitude Summer			
4	0.96	101.282	300	0.7149	25.086	29.367
		116.526	290			
5	0.96	91.243	300	0.5906	42.538	49.802
		106.962	290			

* Skin temperatures based on lowest-level atmospheric temperatures for MODTRAN's midlatitude winter (272 K) and summer (295 K) atmospheres. Two skin temperatures used to simulate satellite radiances measured at two different times.

grass; Pielke 1984) were used for September/June and December/March, respectively.

3. Simultaneous retrieval methodology

a. Optimization scheme

In standard form and with the assumption of time invariant emissivity, FS-98 uses GOES channel-4 and -5 radiances measured at two times along with MODTRAN-calculated channel transmittances and directional radiances to retrieve two channel emissivities (ε_4, ε_5) and two LSTs (T_{s1}, T_{s2}). This is done by optimization that minimizes the sum of squared differences between observed GOES radiances (I_{sat}) and those calculated by the RTE model (I_{rte}) consistent with Eq. (2), and expressed by a cost function $F(\mathbf{X})$:

$$F(\mathbf{X}) = \sum_{\substack{i=4,5 \\ t=1,2}} (I_{\text{sat},i,t} - I_{\text{rte},i,t})^2, \tag{4}$$

where the elements of the vector $\mathbf{X}$ are the four retrieval variables, subscript $t = 1, 2$ refers to observations made at times 1 and 2, and subscript $i = 4, 5$ refers to the two split window channels. The optimization is accomplished with TN-PACK (truncated Newton minimization package) software (Schlick and Folgelson 1992). This system uses a truncated form of Newton's method for optimizing multivariate functions such as given in Eq. (4).

By linearizing the Planck function, Eq. (4) can be solved algebraically. However, slight errors in atmospheric correction plus channel noise in the satellite observations lead to physically unrealistic solutions. Therefore, an optimization approach is used to enable constraints to be placed on the solutions. Field and laboratory measurements show that split-window emissivities of bare soils lie in the range of 0.946–0.972, dry vegetation around 0.949, and green vegetation around 0.985; see Schmugge et al. (1991) and Rubio et al. (1997). Based on these measurements, the lower- and upper-emissivity bounds are set to 0.90 and 0.999, while the skin temperature bounds at time 1(2) are set to be within ±15°C of a channel-4 EBBT at time 1(2).

Each study period contains GOES images collected at N number of times through the course of 12–48 h. To create pairs of images for the retrieval algorithm, the image sets are broken into two groups with the first group consisting of images taken at times 1 through $N/2$ and the second group consisting of images taken at times $(N/2) + 1$ through N. Then the first channel-4/-5 dual image in group 1 is paired with the first channel-4/-5 dual image in group 2, the second dual image in group 1 is paired with the second dual image in group 2, and so on, giving $N/2$ pairings. Applying the algorithm to each pair produces time series consisting of N LSTs and $N/2$ channel-4 and -5 emissivities. Because the study periods are of varying time durations, including short periods of missing data (either because of satellite eclipse or overcast cloud conditions), the amount of time separating images within a pair differs (see last column of Table 2).

b. Sensitivity testing

Analysis of Eqs. (2) and (4) shows that retrieval errors will arise from noise in the satellite radiances and inaccurate atmospheric correction. The latter is due to inexactness in the MODTRAN RTE model, measurement errors in the radiosonde profiles, and interpolation of the atmospheric correction factors with time and over the study area. To understand the potential effects of these errors, a series of sensitivity experiments was performed. For two of MODTRAN's preset atmospheres (midlatitude winter and summer), two sets of channel radiances were generated using skin temperatures differing by ±5°C of the lowest-level atmospheric tem-

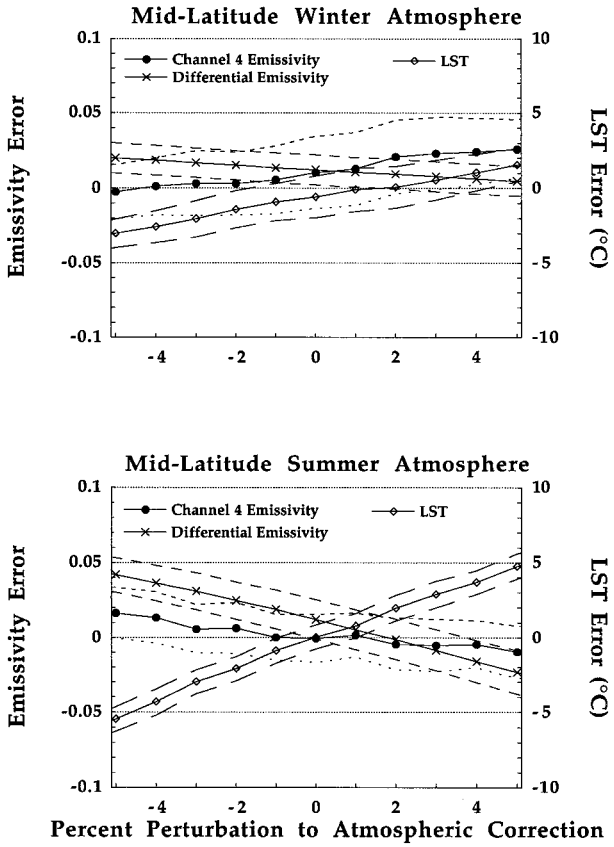

FIG. 1. Results of retrieval sensitivity experiments. Top panel is for midlatitude winter atmosphere; bottom panel is for midlatitude summer atmosphere.

perature (the $\pm$ indicates skin temperature deviations at the two different times) and channel emissivities of 0.96 (see Table 3 for a summary of satellite radiances and atmospheric correction terms). To simulate the combined effects of radiosonde and radiative transfer model errors, the atmospheric correction terms were perturbed by an integer percentage ranging from -5% to $+5\%$. To simulate the effects of satellite noise, a random number generator, producing Gaussian distributions with zero mean and standard deviations equivalent to GOES channels' NEΔNs, was used to produce a set of 100 satellite radiance perturbations for each channel. Retrievals were done separately for each increment of atmospheric correction error using the same set of satellite radiance noise (11 sets of 100 retrievals).

Results for both winter and summer atmospheres are given in Fig. 1. These consist of average LST, channel-4 emissivity, and differential emissivity ($\Delta\varepsilon = \varepsilon_4 - \varepsilon_5$) errors, along with their respective standard deviations for both atmospheres. In this context, an error is found by differencing the retrieval quantity from the truth value. Only the LST curve for time 1 is shown, because the LST errors are nearly identical for times 1 and 2 for both seasons. Differential emissivity error is presented for graphical clarity. (Note, the channel-5 emissivity error can be obtained by adding $\Delta\varepsilon$ to the channel-4 emissivity error.)

Figure 1 shows that the LST and differential emissivity errors both increase according to the magnitude of atmospheric correction error. The magnitude of the summer channel-4 emissivity error has the same behavior as well. Furthermore, the retrieval errors are larger for the summer. This is because absolute errors for the more moist summer atmospheric corrections will be larger than equivalent percentage errors taken in winter. The nonzero average retrieval errors for 0% atmospheric correction error are due to nonzero-averaged satellite radiance noise (the simulated noise has a nonzero average as the sample size increases).

If the reflection term in Eq. (2) is ignored, then it is expected that the LSTs and emissivities will increase (decrease) to compensate any decrease (increase) in atmospheric correction. While the change in the Planck function radiance, $B_i(T_s)$, with LST is approximately the same for both channels, the required changes in surface emittance, $\varepsilon_i B_i(T_s)$, needed to compensate changes in the atmospheric corrections will differ between channels because the radiance (transmittance) is larger (smaller) in channel 5 than in channel 4. The net result is that channel emissivities will adjust differently in the surface emittance term for a given LST change. For the winter atmosphere both emissivities increase (decrease) with decreased (increased) atmospheric correction. This stems from the smaller atmospheric correction differences between channels 4 and 5 related to drier conditions. The larger differences in the summer atmospheric correction terms require the channel-4 emissivities to decrease for negative perturbations. For example, a negative 5% perturbation requires 8.1 and 12.4 mW m^{-2} sr^{-1} increases in surface emittances for channels 4 and 5, respectively. Compare these with the 4.4 and 5.6 mW m^{-2} sr^{-1} increases required for a winter atmosphere. The approximate 6°C LST increase produces approximately equal increases of 10.34 and 10.72 mW m^{-2} sr^{-1} in the Planck function evaluated for channels 4 and 5. It can be seen that such a change is too large for channel 4 while too small for channel 5. To compensate, the channel-5 emissivity increases to 0.975 while the channel-4 value decreases to 0.940. Thus, the behavior of channel-4 emissivity in summer is due to different responses between channels caused by perturbed atmospheric conditions.

4. Validation at seasonal scale

A first-order analysis of the atmospheric correction error, from combined radiosonde-MODTRAN inaccuracies, was done by comparing the calculated downwelling radiances with those measured by the Atmospheric Emitted Radiance Interferometer (AERI) located at the central ARM–CART facility. Averages of the calculated and measured channel radiances, when avail-

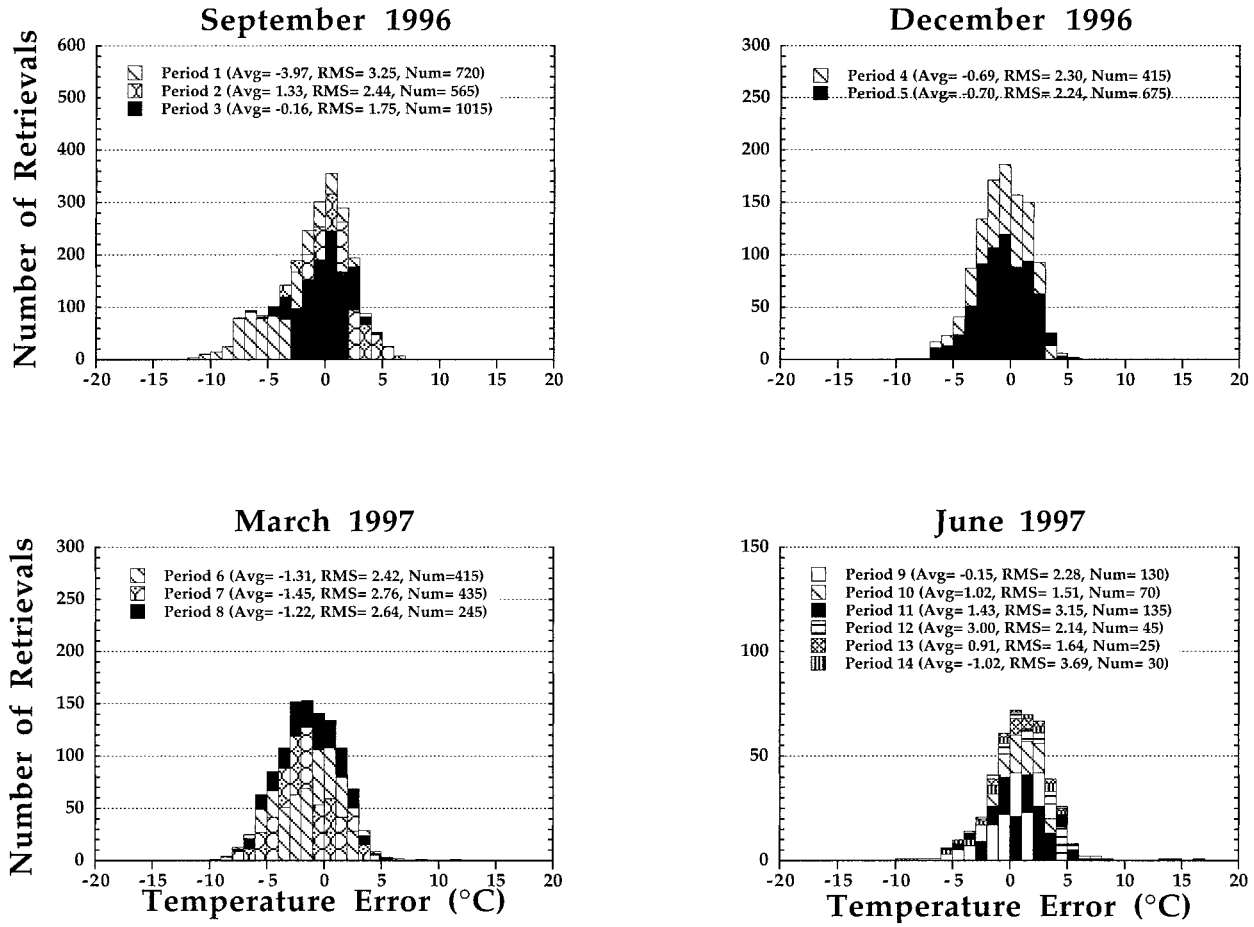

FIG. 2. Monthly histograms of LST retrieval errors (validation − retrieval). Biases, rmses, and number of validation measurements available for each study period are given in upper portions of each panel.

able, are given in Table 1. While the largest errors occur during June, the percentage errors do not show a seasonal trend. As expected, although the differences between the time averages for Period 1 are small, the time series of calculated minus measured radiances (not shown) indicate larger errors, both positive and negative, throughout this study period.

The retrieved LSTs for the GOES pixels closest to each of the validation sites were compared with 10-min averages of the corresponding surface measurements. It should be noted that the spatial scales observed by the GOES and pyrgeometer instruments differ, which may lead to some systematic bias in the intercomparison. Histograms of LST errors (validation minus retrieval) for each study period are given in Fig. 2 along with the associated biases and rmses; these two quantities are less than 1.5° and 2.8°C, respectively, for the 10 study periods.

Because in situ emissivity measurements are not available from ARM–CART, the retrievals must be judged against what has been measured in previous field and laboratory experiments. A GOES pixel in this region generally consists of a mixture of vegetation and exposed soil, especially in the agricultural regions. Valor and Caselles (1996) developed a model for the effective emissivity of a satellite pixel where the emissivity is given as a weighted average of the vegetation (ε_v) and soil (ε_g) emissivities, along with a term that takes into account the internal reflections at the surface ($d\varepsilon$) given by

$$\varepsilon_\lambda = F_v\varepsilon_v + (1 - F_v)\varepsilon_g + d\varepsilon, \qquad (5)$$

where the weights are the complementary fractional vegetation cover (F_v) terms. To estimate the range of emissivities for GOES pixels from Eq. (5), we use measurements of emissivities for soils and vegetation and the expected range of fractional vegetation cover of 0% (for fallow agriculture) to 100% (for full vegetation cover). The $d\varepsilon$ term was not included, because the information needed for its calculation was not available. Schmugge et al. (1991) found soil emissivities ranging from 0.946 to 0.963 for the 10.2–11.2-μm TIMS channel; Rubio et al. (1997) found larger values of 0.969–0.974 with characteristic uncertainties of $\pm$0.006 for the AVHRR 10.5-μm channel. For dry and green vegetation Rubio et al. (1997) give values of 0.949 $\pm$ 0.022 and 0.985 $\pm$ 0.001. Rubio et al. (1997) also found differ-

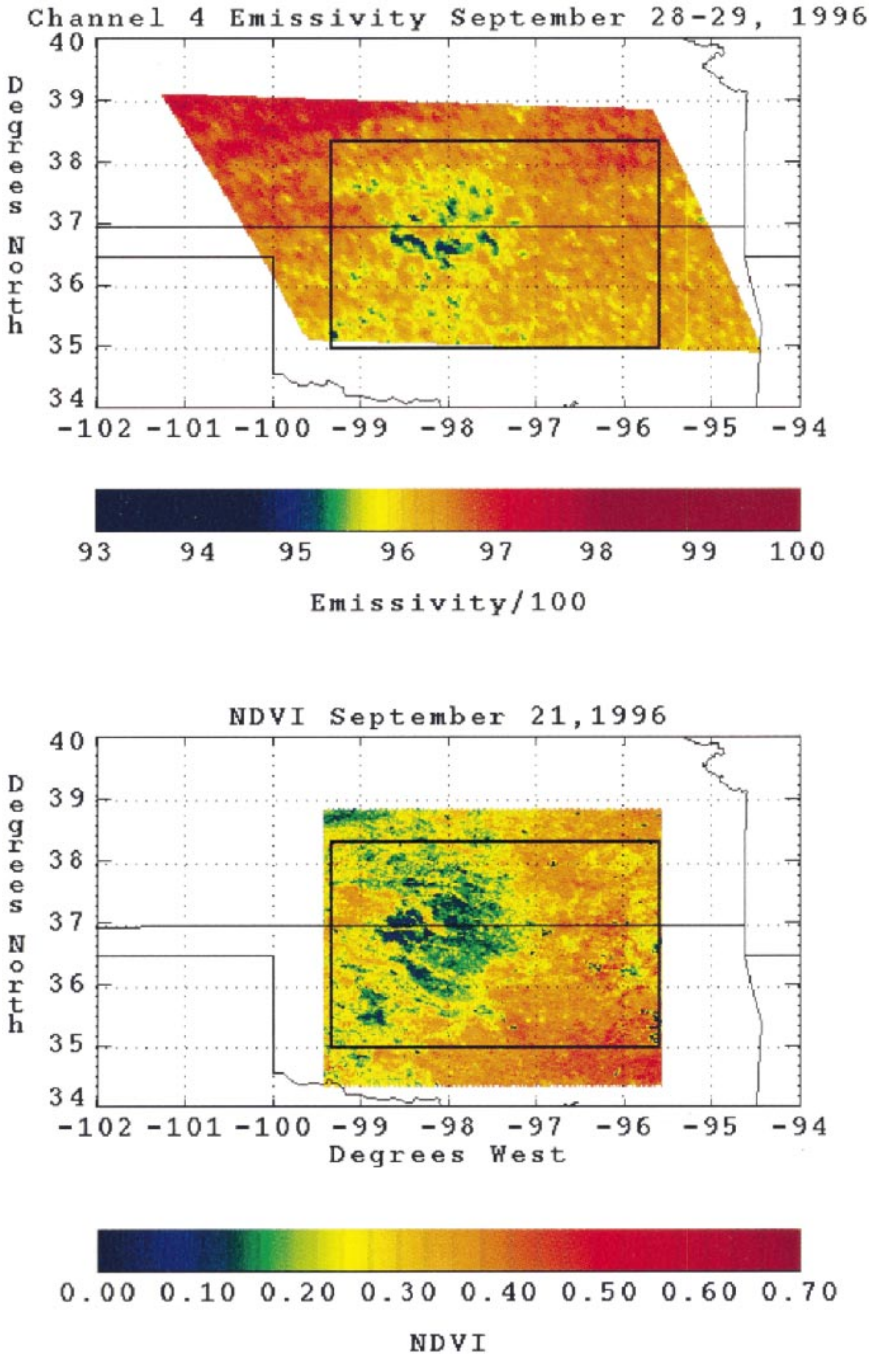

FIG. 3. Top panel is averaged retrieved channel-4 emissivity field for 28–29 Sep 1996 over study area. Bottom panel is retrieved NDVI from *NOAA-14* AVHRR measurements for 22 Sep 1996. ARM–CART boundary is denoted by thick solid line box, lat–long grid by thin dotted lines, and state boundaries by thin solid lines.

ential emissivities of near −0.001 for green vegetation, −0.005 for dry vegetation, and close to −0.08 for soils. From this information the estimated range of channel-4 emissivities for the ''growing'' months (June and September) is 0.946 (0% vegetation cover, using smallest value of bare soil emissivity) to 0.985 (100% vegetation cover). During the senescent winter months when there is little green vegetation, the range is estimated to be 0.949 (100% dry vegetation cover) to 0.974 (0% vegetation cover using largest value of bare soil emissivity).

The time-averaged retrieved channel-4 emissivities for study period 3 are presented in Fig. 3 along with

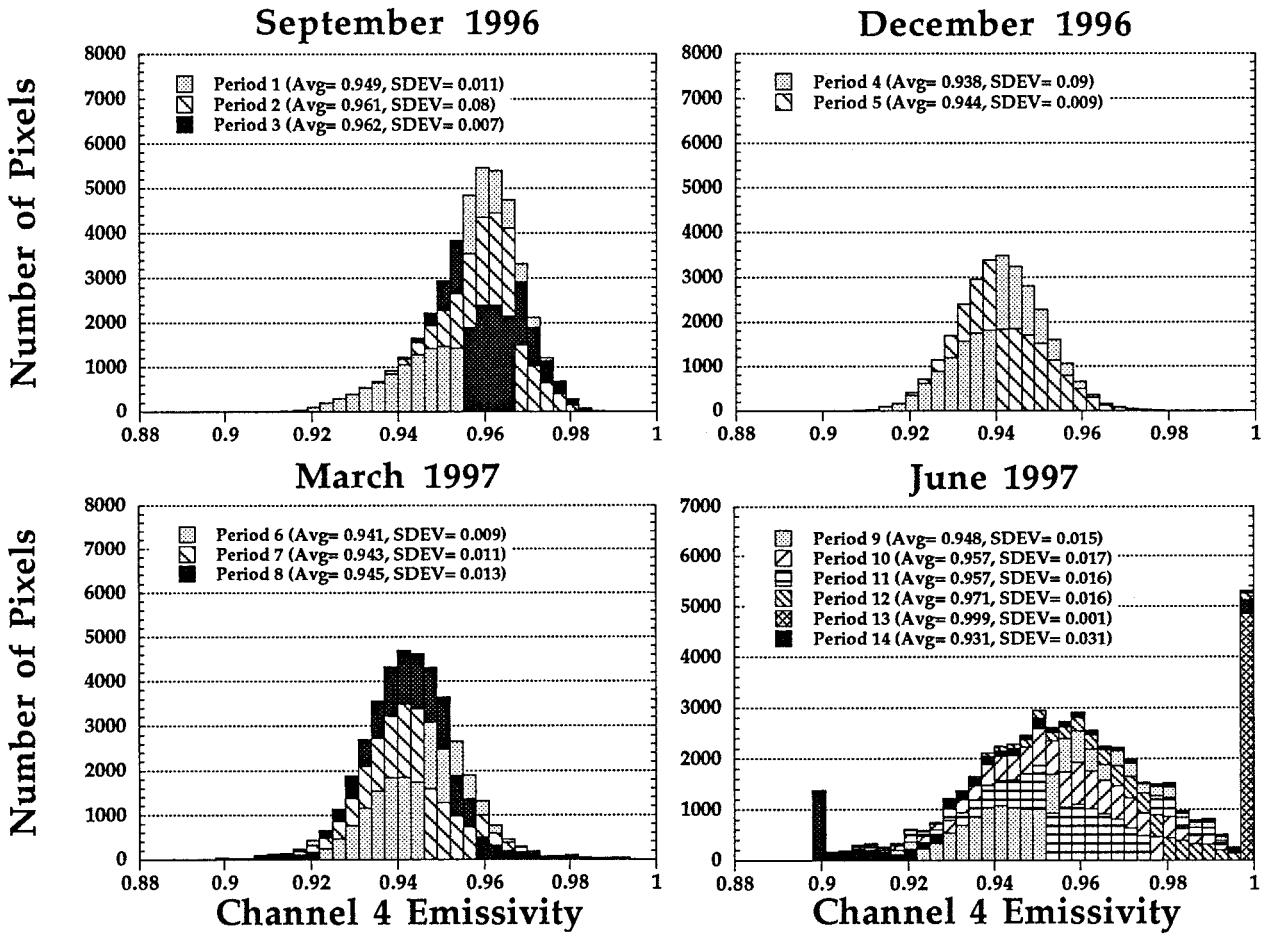

FIG. 4. Monthly histograms of time averaged retrieved channel-4 emissivities for ARM–CART study area. Results are presented in terms of number of pixels rather than frequency, because many Jun satellite images had cloud cover preventing retrieval. ARM–CART satellite images consist of 180 × 80 pixels.

NDVI calculated from *NOAA-14* AVHRR visible and near-infrared measurements obtained a week earlier. NDVI is presented because it is an approximate indicator of fractional vegetation cover. In general, the areas of smallest (largest) emissivities correspond to areas of lowest (highest) NDVI. Gao et al. (1998) indicate that small NDVIs correspond to areas of winter wheat that were harvested at summer's end, while the large NDVIs to the east correspond to areas of rangeland. Emissivities for the harvested areas range from 0.94 to 0.96 while those for the vegetated areas range from 0.96 to 0.98, agreeing with the above soil and vegetation emissivities.

Histograms of the retrieved channel 4 and differential emissivities for all study periods are presented in Figs. 4 and 5. There is a seasonal cycle in emissivity with an average value of ~0.96 for September, ~0.942–0.943 for December and March, and ~0.96 for several June study periods. Based on NDVI maps from Gao et al. (1998), the emissivity characteristics are consistent with the seasonal cycle in green vegetation cover.

The retrieved channel-4 emissivities were slightly smaller than expected for the individual months. For example, the December average of 0.942 was less than the low end of the senescent month range (0.949). Although the average differential emissivities were close in magnitude to the Rubio et al. (1997) measurements, the histograms show a number of retrievals having large differential emissivities (greater than 0.01 in magnitude), especially in the June and early-September study periods. These types of errors are consistent with the results from the sensitivity experiments where the retrieved channel-4 emissivities were typically small while the differential emissivities increased with percentage atmospheric correction error (i.e., as the atmosphere becomes warmer and moister). Retrieval results improve insofar as LST biases and rmses, spreads in retrieved channel-4 emissivities, and differential emissivities improve as the atmosphere becomes drier and cooler. This can be seen by comparing June and early-September results to those from December, March, and late September; the former contain the largest percentage atmospheric correction errors.

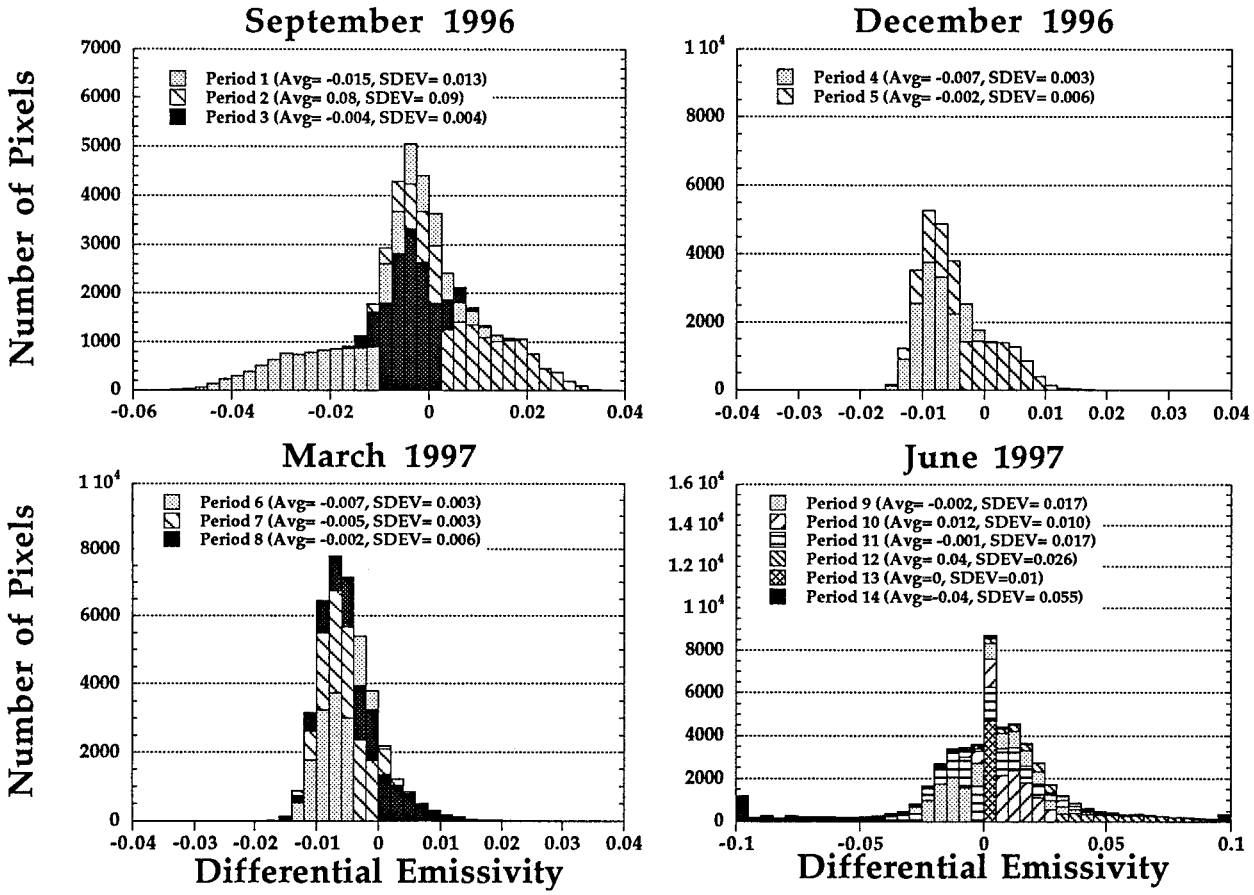

FIG. 5. Same as Fig. 4 except for time-averaged retrieved differential emissivities.

5. LST–emissivity properties at ARM–CART domain scale

Area-averaged LSTs along with the +/− standard deviations for ARM–CART are presented in Fig. 6, composited over one study period per season. The LSTs exhibit the expected seasonal and diurnal behavior with seasonal maxima (minima) occurring in June (December) and a diurnal pattern consisting of a half-wave sinusoidal oscillation during the day and a slow linear decrease at night. An interesting aspect of the June and September study periods is that the temperatures are warmer on the second day of the periods. For example, on 29 September the temperatures are warmer with a diurnal amplitude 3°C greater than on 28 September. This behavior is due to the large-scale synoptic weather conditions in which overcast conditions prior to the study period impeded the surface radiative forcing. On the second day of period 3 the surface had already experienced a full day of nearly clear-sky heating (i.e., on 28 September).

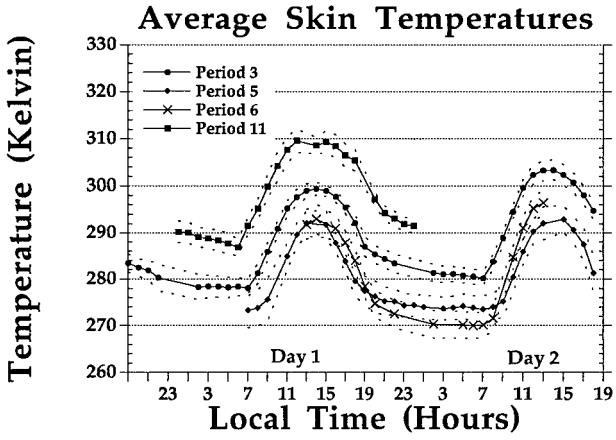

FIG. 6. Time series of area-averaged LSTs over entire study area for several study periods; ± unit standard deviation spreads are indicated by dashed lines.

The large-scale average results presented in Fig. 6 would be useful for representing the ARM–CART domain as a grid point in conjunction with a large-scale weather model. However, there are additional diurnal and seasonal variability details in the surface temperature fields that are useful in diagnosing mesoscale processes over the study area. To illustrate, September- and March-averaged noon and midnight LST images are presented in Fig. 7. These images were created by av-

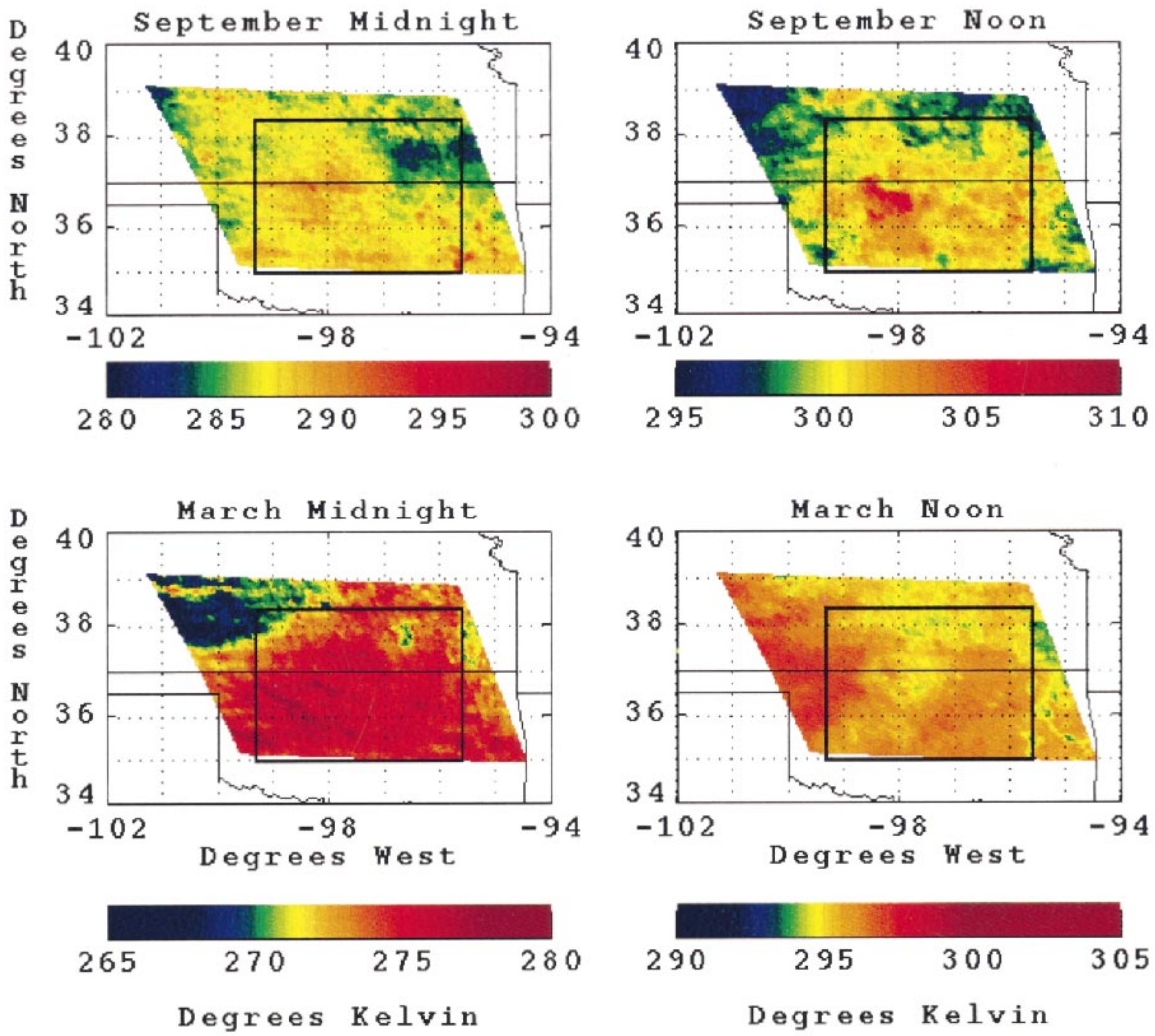

FIG. 7. Composite midnight and noon LST images for Sep 1996 and Mar 1997. ARM–CART boundary is denoted by thick solid line box, lat–long grid by thin dotted lines, and state boundaries by thin solid lines.

eraging the retrieved LSTs for the 3-h periods centered around noon and midnight. Note that most of the September midnight sequence was missing because of satellite eclipse conditions. Because the nighttime temperatures exhibit near linear decrease (as in Fig. 6), the 3-h midnight period for September was approximated by averaging the 2215 and 0215 local time retrievals. Note that the color scales differ for each of the four panels in Fig. 7, emphasizing the varying dynamic ranges of LSTs during each period.

There are distinct diurnal and seasonal shifts in the temperature patterns for these two months as well as for December and June (not shown). In September the warmest LSTs are concentrated toward the center of the study area while the coolest nighttime LSTs are found along the western fringe and in the northeast corner. The coolest daytime LSTs are concentrated in two areas north of 37°N. In December the warmest nighttime LSTs are concentrated to the southeast with coolest LSTs in the northeast and northwest corners. Daytime LSTs exhibit a more north to south gradient increase.

The coolest nighttime LSTs for March are concentrated in the northwest with a fairly even distribution across the remainder of the image. The daytime LSTs are warmest along the western side of the image, with the coolest LSTs toward the center and along the eastern portion. This is a complete reversal of the September pattern when the maximum LSTs are located near the center of the domain. By June the coolest nighttime LSTs are along a swath north of 38°N, in an area on the eastern side of the study area. It was difficult to judge the June noon retrievals since there was a sizable amount of cloud cover at the time, but there appears to be an increase in LSTs from east to west (also seen at midnight). Gao et al. (1998) reported a similar orien-

tation of LSTs retrieved from the Price (1984) LST algorithm.

The seasonal behavior of the ARM–CART emissivity fields was discussed in section 4 in conjunction with the retrieval validation. The underlying premise was that the emissivity behavior should follow the seasonal cycle in vegetation cover with the nonsenescent months exhibiting greatest emissivities. The retrieved emissivities follow this trend with June and September indicating the largest values.

6. Conclusions

This study has described the behavior of simultaneously retrieved LSTs and thermal infrared window emissivities across the ARM–CART experimental area for a sequence of four months extending from September 1996 to June 1997. The retrieval algorithm uses *GOES-8* split window measurements at two sample times 6–24 h apart to determine two LSTs and two spectral emissivities (considered to be invariant across the sampling time interval). Analysis of the results emphasizes the seasonal cycle in the emissivities caused by changing surface cover conditions and the diurnal to seasonal cycles in the site-averaged LSTs from varying solar radiative forcing. Averages of the retrievals centered around noon and midnight show seasonal changes in the LST distribution.

The sensitivity analysis and retrieval results show that the accuracy of the retrievals improves as the columnar water vapor paths and average atmospheric temperatures decrease. On 9–11 September and for much of June (primarily the last 4 periods) the averaged differences between the retrieved and in situ temperatures and retrieved differential emissivities were larger than during any of the other 14 study periods. At the same time, the precipitable water content was 1.0–3.0 cm larger than in the other study periods. The improved results during the late September and winter study periods are due to more accurate atmospheric corrections, governed by minimal percentage errors in atmospheric transmission during cool and dry periods.

Based on the results of this study, the optimal conditions for simultaneous retrieval would be for water vapor paths generally less than 2.5 cm and average atmospheric temperatures less than 290 K. These values are generally below those of warmer, more tropical environments, and thus the technique leads to greater uncertainties when extending its application globally. However, the same types of limitations are found with the physical versions of the standard LST algorithms because they all assume linear relationships between precipitable water and split window transmissions, an assumption that deteriorates as water vapor paths increase and the transmissions tend toward their exact exponential form. However, emissivity retrieval is most relevant to semiarid and arid regions where fractional vegetation covers are consistently less than 1.0 and soils are exposed, because these are the surfaces that exhibit the greatest emissivity and differential emissivity variability, as well as the greatest differential emissivity itself. From this perspective, there is a definite role for simultaneous LST–emissivity retrieval in current operational meteorology.

Acknowledgments. The authors wish to thank James Lamm for his assistance with the computer graphics as well as the constructive advice of two anonymous reviewers. ARM–CART data were obtained from the Atmospheric Radiation Measurement Program sponsored by the U.S. Department of Energy, Office of Health and Environmental Research, Environmental Sciences Division. This research was supported by a graduate fellowship from the American Meteorological Society, NASA Global Change Fellowship NGT5-30116, and NASA Research Grant NAG5-6258.

REFERENCES

Becker, F., 1987: The impact of spectral emissivity on the measurement of land surface temperature from a satellite. *Int. J. Remote Sens.,* **8,** 1509–1522.

——, and Z.-L. Li, 1990: Towards a local split window method over land surfaces. *Int. J. Remote Sens.,* **11,** 369–393.

Berk, A., L. S. Bernstein, and D. C. Robertson, 1989: MODTRAN: A moderate resolution model for Lowtran 7. Spectral Sciences, Inc., Tech. Rep. GL-TR-89-0122, 38 pp. [Available from Spectral Sciences, Inc., 99 South Bedford St., No. 7, Burlington, MA 01803.]

Caselles, V., C. Coll, and E. Valor, 1997: Land surface emissivity and temperature determination in the whole HAPEX-Sahel area from AVHRR data. *Int. J. Remote Sens.,* **18,** 1009–1027.

Faysash, D. A., and E. A. Smith, 1999: Simultaneous land surface temperature–emissivity retrieval in the infrared split window. *J. Atmos. Oceanic Technol.,* **16,** 1673–1689.

Gao, W., R. L. Coulter, B. M. Lesht, J. Qiu, and M. L. Wesely, 1998: Estimating clear-sky regional surface fluxes in the southern Great Plains Atmospheric Radiation Measurement site with ground measurements and satellite observations. *J. Appl. Meteor.,* **37,** 5–22.

Kidder, S. Q., and T. H. Vonder Haar, 1995: *Satellite Meteorology.* Academic Press, 466 pp.

Li, Z.-L., and F. Becker, 1993: Feasibility of land surface temperature and emissivity determination from AVHRR data. *Remote Sens. Environ.,* **43,** 67–85.

Nerry, F., J. Labed, and M. P. Stoll, 1990: Spectral properties of land surface in the thermal infrared. 2: Field method for spectrally averaged emissivity measurements. *J. Geophys. Res.,* **95,** 7045–7062.

Pielke, R. A, 1984: *Mesoscale Meteorological Modeling.* Academic Press, 611 pp.

Prata, A. J., 1994: Land surface temperatures derived from the Advanced Very High Resolution Radiometer and the Along-Track Scanning Radiometer: 2. Experimental results and validation of AVHRR algorithms. *J. Geophys. Res.,* **99,** 13 025–13 058.

——, V. Caselles, C. Coll, J. A. Sobrino, and C. Ottlé, 1995: Thermal remote sensing of land surface temperature from satellites: Current status and future prospects. *Remote Sens. Rev.,* **12,** 175–224.

Price, J. C., 1984: Land surface temperature measurements from the split window channels of the *NOAA-7* Advanced Very High Resolution Radiometer. *J. Geophys. Res.,* **89,** 7231–7237.

Rubio, E., V. Caselles, and C. Badenas, 1997: Emissivity measure-

ments of several soils and vegetation types in the 8–14 μm wave band: Analysis of two field methods. *Remote Sens. Environ.,* **59,** 490–521.

Schlick, T., and A. Fogelson, 1992: TNPACK–A truncated Newton minimization package for large-scale problems. I: Algorithm and usage. *ACM Trans. Math. Software*, **18,** 46–70.

Schmugge, T. J., F. Becker, and Z. L. Li, 1991: Spectral emissivity variations observed in airborne surface temperature measurements. *Remote Sens. Environ.,* **35,** 95–104.

Stokes, G. M., and S. E. Schwartz, 1994: The Atmospheric Radiation Measurement (ARM) Program: Programmatic background and design of the Cloud and Radiation Test Bed. *Bull. Amer. Meteor. Soc.,* **75,** 1201–1221.

Valor, E., and V. Caselles, 1996: Mapping land surface emissivity from NDVI: Application to European, African, and South American areas. *Remote Sens. Environ.,* **57,** 167–184.

Watson, K., 1992: Two-temperature method for measuring emissivity. *Remote Sens. Environ.,* **42,** 117–121.

Xiang, X., and E. A. Smith, 1997: Feasibility of simultaneous surface temperature–emissivity retrieval using SSM/I measurements from HAPEX-Sahel. *J. Hydrol.,* **188–189,** 330–360.